

Synthetic Augmentation pix2pix using Tri-category Label with Edge structure for Accurate Segmentation architectures

Yasuno Takato
Yachiyo Engineering, Co.,Ltd.
5-20-8, Asakusabashi, Taito-ku, Tokyo.
tk-yasuno@yachiyo-eng.co.jp

Abstract

In medical image diagnosis, pathology image analysis using semantic segmentation becomes important for efficient screening as a field of digital pathology. The spatial augmentation is ordinarily used for semantic segmentation. Images of malignant tumor are rare, and annotating the labels of the nuclei region is a time-consuming process. An effective use of the dataset is required to maximize the segmentation accuracy. It is expected that augmentation to transform generalized images influences the segmentation performance. We propose a “synthetic augmentation” using label-to-image translation, mapping from a semantic label with an edge structure to a real image. This paper deals with the stain slides of nuclei in tumor. We demonstrate several segmentation algorithms applied to the initial dataset that contains real images and labels using synthetic augmentation in order to add their generalized images. We compute and report that a proposed synthetic augmentation procedure improves the accuracy indices.

1. Introduction

1.1. Semantic segmentation for pathology image analysis

Microscopic pathology slides can capture the histologic details of tissues with a high resolution. Owing to the rapidly advancing technology, the whole-slide imaging (WSI) becomes part of the ordinary procedure for clinical diagnosis of various diseases. Automating image analysis accurately and efficiently remains a challenge. Recently, deep learning algorithms have shown great promise in pathology image analysis, such as in tumor region identification, metastasis detection, and patient prognosis. Many deep learning algorithms, including fully convolutional networks (FCN), U-Net, and newer inspired architectures, have been proposed to automatically segment pathology images. Among these algorithms, segmentation deep learning algorithms, such as fully convolutional networks, are well known for higher accuracy, computational efficiency, and end-to-end learnability. Thus, pathology image semantic segmentation has become a practical tool in WSI analysis.

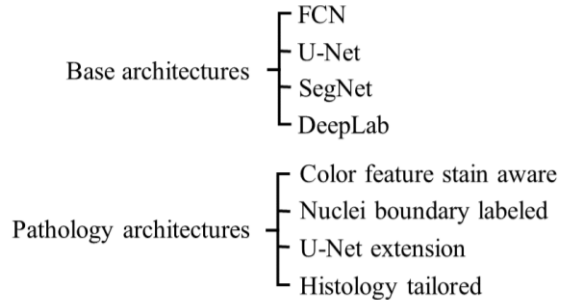


Figure 1: Deep learning architecture for pathology image segmentation (tissue, nuclei, glands, tumor)

Wang et al. reviewed the applications of deep learning algorithms for pathology image segmentation in WSI image analysis [1]. They pointed toward image preprocessing that entails image normalization, shape augmentation, and color augmentation. There are several image-shape augmentation methods, such as a projective matrix transformation, which involves scaling, translation, rotation, and affine transformations. The color augmentation is important to make the deep learning algorithm learn to adapt features, because pathology image may look very different owing to different staining conditions and slide thickness. For example, hematoxylin and eosin (H&E)-stained renal cell carcinoma pathology images are often classified into eosinophilic and basophilic subtypes, which are prone to be stained by eosin (magenta) or hematoxylin (blue), respectively, and thus have intrinsically different color distributions. There are several color augmentation methods, such as adding a random mean, multiplying a random variation to each channel of each image, adding Gaussian noise, and so forth.

As shown in Figure 1, there are useful architectures for pathology image analysis, such as semantic segmentation algorithms using deep learning. The first end-to-end and pixel-to-pixel semantic segmentation neural network is the fully convolutional network (FCN) [2]. Many modifications have been made to FCN to further improve the segmentation performance. For example, U-Net [3] greatly increases the number of deconvolutional layers to propagate information to higher resolutions with convolution and max-pooling layers demonstrated in medical images. SegNet [4] refines

the encoder-decoder network layers with skip connections, including typically three layers: convolution, batch normalization, and ReLU. Recently, DeepLab replaced the deconvolutional layers with atrous (densely) convolution and atrous spatial pyramid pooling instead of standard convolution layers [5].

Inspired with this base network, there are many proposed deep neural networks for pathology image segmentation frameworks, such as color feature stain aware model [6][7], nuclei boundary-labeled model [8][9], U-Net extension model [10], and histology tailored model [11][12]. From a task point of view, since 2017, Dabass et al. reviewed 20 pathological image segmentation studies using deep learning, which involved tissue, nuclei, glands, tumor, and various segmentations that were applied to different pixel size input images and their accuracy measures such as Precision, Recall, F1-score, and Dice coefficient (Intersection of Union; abbreviate IoU) [13]. However, we face a challenge of achieving higher performance and accuracy for the pathology image segmentation. More effective augmentation procedure is required for computational pathology practitioners.

1.2. Synthetic image augmentation using generative models

Since 2014, the original generative adversarial network (GAN) paper has been cited more than 9,000 times to date (July 2019). Starting from GAN's introduction in 2014, the field of GAN has been growing exponentially, with over 360 papers written on it [14]. Yi et al. reviewed GAN related 150 papers in medical imaging before January 2019. [15]. Here, used algorithms were categorized as synthesis (46%), reconstruction (20%), segmentation (17%), classification (8%) and others. Also the domain were categorized such as MR (43%), CT (20%), histopathology (9%), X-ray (8%) and so forth. For examples, there are domain specific studies for the skin lesion segmentation [16][17]. However, the technical merit of synthetic augmentation is not understood. The segmentation studies for pathology analysis just started.

GANs may be used for various applications, not just for fighting breast cancer or generating human faces, but also for 62 other medical GAN applications published through the end of July 2018 [18]. Using DCGAN for data augmentation, a significant improvement in classification accuracy compared to the baseline of standard data augmentation only was achieved [19]. The medical dataset were generated by their DCGAN, after which the classification performance improved from around 80% to 85%, demonstrating the usefulness of GANs. However, we do not know yet for sure whether generative synthetic augmentation could improve performance or not. In pathology image analysis, such segmentation accuracy becomes important for diagnosis and prognosis. We often require annotating the nuclei region of interest as a semantic

label, which requires heavy workforces and a longer duration of time.

In order to overcome the scarcity of images of malignant tumors captured, and the effective use of existing dataset, we have opportunities to generalize the feature of the initial dataset using the generative synthetic augmentation procedure. We propose a generative synthetic augmentation method to improve the performance of the semantic segmentation task during pathology image analysis. We demonstrate the ability of several base architectures to learn the initial dataset and the generative synthetic images using L1-Conditional GAN.

2. Generative synthetic augmentation

2.1. Synthetic image augmentation using GAN

We assume that the approaches for generating a stained slide image include (1) reproducing the already acquired tumor image (similar augmentation), (2) generating a future image degraded from the current damage grade (What-if degradation), and (3) what-if newer damage that does not yet exist (what-if newer). Here, (1) is close to data augmentation that has been performed as standard in supervised learning by rotation, X/Y translation, scaling, and so forth.

In case of (2), it is possible to simulate the situation where the deterioration has progressed several years ahead of the current state. The degraded state that has not yet been experienced, but generates an image of the state that has progressed to one-rank deterioration or the worst image when the management level is low, exceeds the scope where the supervised data exists. This is an attempt to eliminate any blind spots in the supervised learning. The (3) approach was not possible with supervised learning based on the experience data. Even in the case of infrastructures that have not deteriorated, a new damaged image can be generated in order to prepare for future deterioration, and even if it has not yet been experienced, it enables imagining a degraded future image.

However, it is necessary to have clarity about where and how much of the tumor occurs in the stained images. This means that after acquiring the images of the potential tumor through histopathology, it is necessary to design a new possible tumor scenario and place the malignant nuclei at the possible position. It is necessary to generate a potential tumor image with ethics without reality, so as to avoid producing exaggerated fake image. As shown in Figure 2, we propose two synthetic augmentation methods. First, we propose generating a synthetic tumor image dataset using the first replica method 1) of reproducing the current tumor images (we call it "replica synthetic augmentation"). Second, we propose generating another hybrid augmentation method

using both the standard shape augmented and the generative synthetic augmented procedure. Here, the shape augmentation stands for several well-known preprocesses, such as rotation, X-axis reflection, upscale resize, and random cropping (we call it generative “shape synthetic augmentation” method).

2.2. Semantic segmentation architecture

In order to recognize the damage region of interest for social infrastructure, semantic segmentation algorithms are useful. We propose a synthetic augmentation method to generate fake images and labels using the L1-conditional GAN (pix2pix) to translate a label image with a structure edge to a damaged image. We apply several existing per-pixel segmentation tasks based on transfer learning, such as the FCN [2], U-Net [3], SegNet [4], and the dense convolution networks such as the DeepLabv3+ResNet18, ResNet50 [5]. Among other candidate of backbones on the DeepLabv3+ architecture, as far as we try to compute the nuclei segment dataset, it could not improve their performance.

We compare the trained segmentation accuracy using initial dataset with the re-trained segmentation accuracy using synthetic augmentation-added generated images. We evaluate the task performance to compute the similarity indexes between the ground truth damage region of interest (ROI) and the predicted region. Furthermore, we compute the mean intersection of inion (mIoU) and class-IoU that consists of the ROI and background. In order to analyze the property of synthetic augmentation, we compute the precision, recall, and BF score. Therefore, using these existing segmentation algorithms, we evaluate whether our method of synthetic augmentation can improve their segmentation accuracy or not.

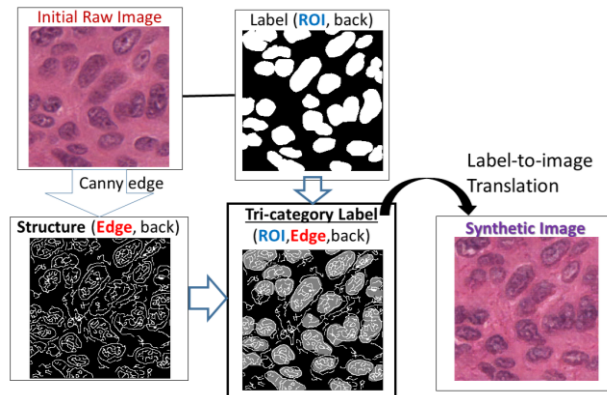


Figure 2: Synthetic augmentation method using label-to-image translation on a nuclei in tumor stained tissue example.

2.3. Label-to-image translation mapping from semantic label with structure edge to tumor image

To train the DCGAN, we need more than 500 images with stable angle. In pathology image analysis on some disease process, a progressed tumor is a rare event, and it is not easy to collect tumor images more than even several hundreds. On the other hand, the image-to-image translation is possible for training a paired image dataset even with various inspection angles. This paper proposes a synthetic augmentation method using L1-Conditional GAN (pix2pix). The original pix2pix paper translated from the input of edge images to shoe images [20]. Using the CamVid dataset, Isola et al. translated from the semantic label to photo. However, in the case of damage images, we could not achieve success, such as achieving naive translation. As shown Figure 2, this paper proposes the semantic label with a structure edge as an input of tri-categorical labels. This augmented label consists of damage-ROI, enhanced structure edge, and background. We tried several edge-detection methods, such as gradient operators (Roberts, Prewitt, Sobel), Laplacian of Gaussian (LoG), zero crossing, and Canny edge, [21]. This paper proposes the Canny edge method to extract the nuclear structure from tumor images. We combine both semantic label and structure edge produced by the Canny edge detection into three class categorical label. We train the mapping from the semantic label with a structure edge to the tumor image.

As shown in Figure 2, we summarize a generative synthetic augmentation step as follows. First, we train a semantic segmentation task using the initial dataset, including tumor images and the semantic label. Second, we apply our replica and shape synthetic augmentation methods mapping to generate near-real images using L1-Conditional GAN from combined semantic label with a structure edge. Third, we re-train another semantic segmentation task using both the initial dataset and our generated near-real tumor images dataset. The number of datasets is two or three times compared with the initial dataset, so as to extend an opportunity to learn the ROI and the background feature between real tumor slide image and fake synthetic images.

3. Pathology image segmentation study

3.1. Nuclei in tumor dataset

We use an open accessed dataset [9], which is the cancer tumor images and nuclei annotated labels. As shown in Figure 3, they are stained hematoxylin and eosin (H&E) images of 40x magnification. The dataset is partitioned with the 30 training images and the 14 test images. Kumer et al. [9] downloaded 30 whole-slide images of digitized tissue samples of several organs from The Cancer Genomic Atlas (TCGA) [22]. These images came from 18 different

hospitals. The training whole-slide images contain four organ sub-types, breast, liver, kidney, and prostate, while the test images include three organ sub-types, bladder, colon, stomach; these are different nuclei features and backgrounds from the training data.

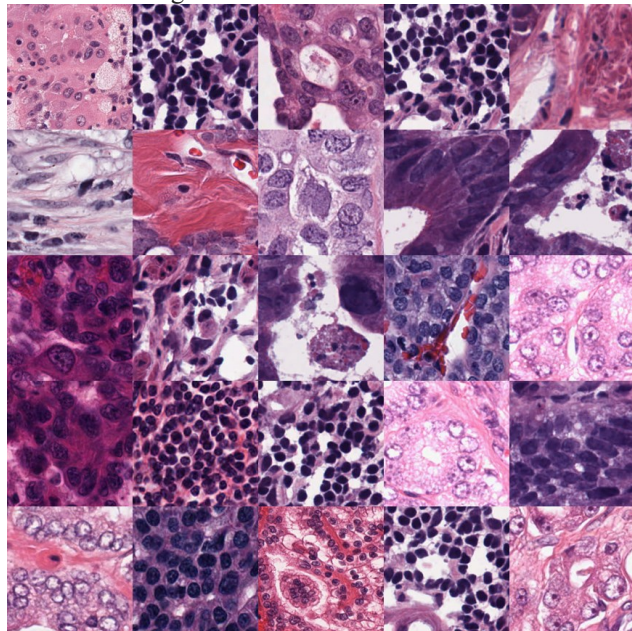


Figure 3: Initial raw tumor images shuffle partially 25 selected from training dataset, where 30 raw images with size 1,000x1,000 pixels were extracted 480 block images sized 250x250 pixels. This dataset is opened at the website by Kumer, N., Verma, R. et al. [9].

Their dataset is annotated by Kumer et al. [9] into the nuclei region of interest (ROI) and two-class background labels over each raw tumor image for nuclei segmentation. Each label has two categories, nuclei ROI (value 255) and background (value 0). The initial raw tumor image has a whole-image size of 1,000 by 1,000. In order to retain the pixel feature, we prepare to extract 4 by 4 block images unified with size 250 by 250, so as to learn standard segmentation architecture to match the input size of 224 by 224. After preparing these, we have an initial training dataset with 480 images and labels. The total background pixel count is 45,564, while the total nuclei pixel count is 15,892. We compute two class weights: the nuclei-ROI is 1.933 and background is 0.674 divided by the median of pixel count on the dataset.

3.2. Generate nuclei images using GAN

We applied the generative synthetic augmentation to the 480 tumor block-image dataset based on the L1-Conditional GAN (pix2pix) [20]. We carried out label-to-image translation from tri-categorical labels combined with the semantic nuclei-ROI and the structure edge by Canny edge operation into the real block tumor

images. As showed in Figure 4, the input tri-label has three categories that contain the structure edge (value 255), the nuclei-ROI (value 128), and the background (value 0), respectively. The output size is 256 by 256 by 3. We trained 200 epochs that took 19 hours. The L1 penalty coefficient is 100 at the loss function.

Figure 5 shows the loss of generator over training process of L1-conditional GAN, where the moving average is 50 iterations to reduce the complexity of plot. After it is repeated at around 55 thousands iterations, that is, 115 epochs, the value of the generator loss is reached at the minimum and stable level.

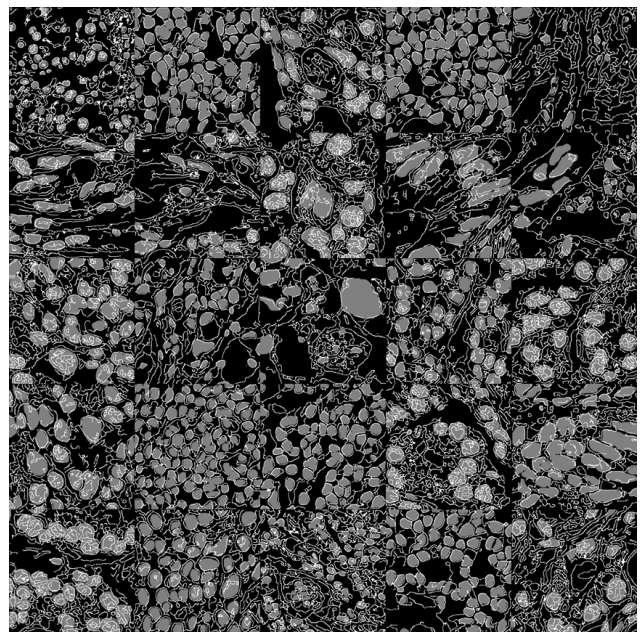


Figure 4: GAN-Input labels with tri-category that contains the Canny edge structure (white color), the region of interest (ROI) of nuclei (silver color), and background (black color) in tumor.

On the other hand, Figure 6 shows the loss of discriminator over the training process of L1-conditional GAN. At the left-half stage, the loss of discriminator decreases at 0.1 level so as to evade the weak synthetic tumor image. After it is repeated for 30,000 iterations, the discriminator loss value approaches the real/fake trade-off movement so as to generate elaborated images that are almost the same as the real tumor images.

Figure 7 shows the generated output images using the generative synthetic augmentation. As compared with Figure 3, these generative synthetic outputs are very similar to the initial raw tumor images. Almost all features of the nuclei-ROI are mapped from the original feature to the synthetic output features such as nuclear shape and stained color of hematoxylin and eosin, respectively.

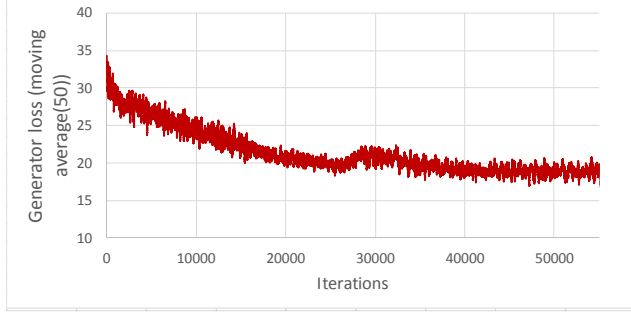


Figure 5: Generator loss over training process of GAN

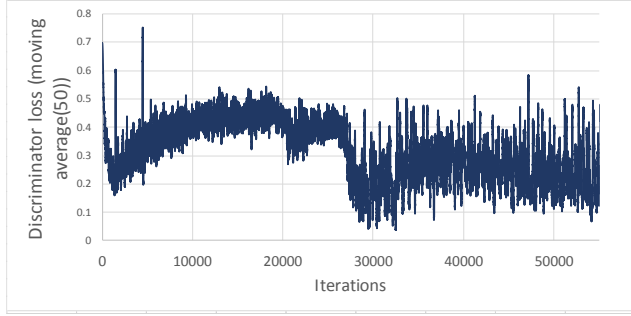


Figure 6: Discriminator loss over training process of GAN

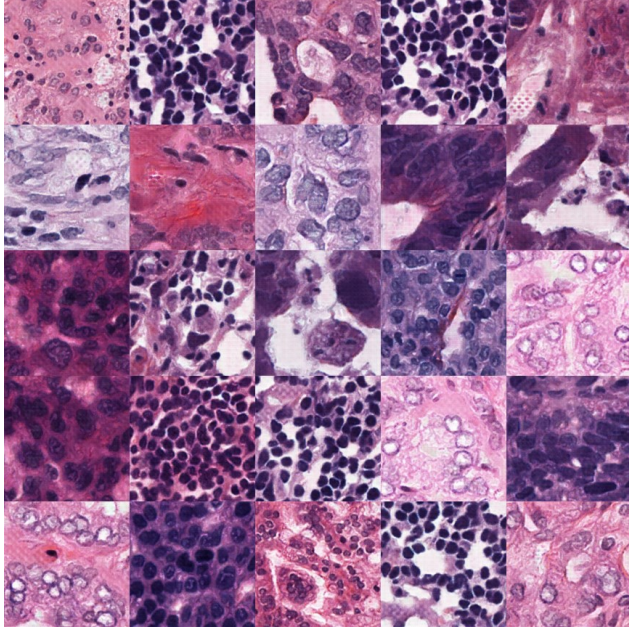


Figure 7: Generated tumor images using generative synthetic augmentation based on L1-Conditional GAN.

3.3. Comparison of the initial set with synthetic augmentation

First, we trained the initial dataset using RMSProp optimizer of 50 to 100 epochs with a mini batch of 8 to 16, that is, around 3000 to 6000 iterations. We performed standard augmentation, such as color jitter, rotation range

-30 to 30, scaling from 0.8 to 1.2, cropping size 224 by 224 pixels, and X-axis reflection. We partitioned the dataset whose weight train versus test is 95:5; each number of the dataset consists of 456 and 24. Second, we trained the added dataset with the 480 generated images using our replica generative synthetic augmentation with the total number of 960, so as to compare the initial result where we set the same epochs. Third, we trained the further added dataset with another 480 generated images using our shape synthetic augmentation with the total number of 1,440, that consists the initial real images and two synthetic augmented images, such as the replica synthetic augmentation, and the shape synthetic augmentation.

Table 1: Trained and test predicted results of intersection of union.

architecture	augmented dataset	run time	F1-score	mean IoU	ROI-IoU	backgrd-IoU
FCN-8s	initial	109m	0.6756	0.7230	0.6202	0.8258
	+replica(G0)	200m	0.7266	0.7553	0.6601	0.8504
	+shape(G1)	323m	0.5553	0.5522	0.4989	0.6054
U-Net	initial	53m	0.7919	0.7778	0.6858	0.8698
	+replica(G0)	110m	0.8488	0.8237	0.7483	0.8991
	+shape(G1)	193m	0.8817	0.8509	0.7876	0.9143
SegNet-VGG16	initial	55m	0.9867	0.9089	0.8687	0.9491
	+replica(G0)	102m	0.9918	0.9283	0.8941	0.9625
	+shape(G1)	202m	0.9870	0.9351	0.9044	0.9658
DeepLabv3+ResNet18	initial	15m	0.9438	0.8854	0.8349	0.9359
	+replica(G0)	26m	0.9632	0.9024	0.8562	0.9485
	+shape(G1)	38m	0.9653	0.9044	0.8604	0.9485
DeepLabv3+ResNet50	initial	31m	0.9830	0.9249	0.8903	0.9594
	+replica(G0)	58m	0.9855	0.9289	0.8944	0.9634
	+shape(G1)	95m	0.9869	0.9356	0.9862	0.9875

Table 1 shows the trained results consisting each running time, F1-score, mean IoU, class-IoU (nuclei region of interest and background). The second run time added with the replica synthetic augmented images, that is “+replicaG0”, took around two times more than the initial dataset. The third run time added with the shape synthetic augmentation, represented by “+shapeG1”, computed over three times.

Regarding F1-score, base architectures such as the FCN, U-Net, SegNet based on VGG16, and DeepLabv3+ based on ResNet18 and ResNet50, show higher values using our generative synthetic augmentation methods, though we exclude the case of FCN-8s +shape(G1). Furthermore, the mean IoU index value indicated that our generative synthetic augmentation out-performs the initial dataset-trained accuracy. Furthermore, the values of the nuclei-ROI class-IoU and background-IoU are the same. Therefore, we propose that our generative synthetic augmentation using L1-Conditional GAN, when applied to the above standard base architectures, improves their segmentation accuracies.

3.4. Predict test images under the initial dataset

We predicted the test dataset of 30 slides, which is the four organ of the training dataset. We tried to predict these block test images with the number of 480, that equals 16 multiply 30, where we prepare to extract the 16 block images with 250 by 250 pixels from the 30 whole slide images with size 1,000 by 1,000 pixels. The weight between train and test is 95 : 5, so the number of test images is 24. The test images are shuffle sampling with fair variations.

Figure 8 shows the four raw tumor images and nuclei ROI labels sampled from the initial dataset, they are typical four organ sub-type within their training dataset.

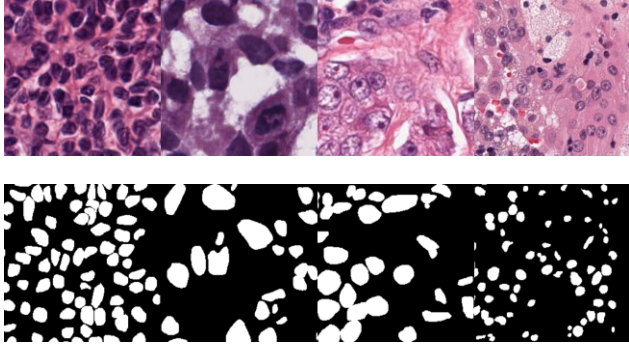


Figure 8: Raw tumor images and nuclei ROI labels, typically sampled from the initial test dataset.

Table 2: Test prediction beyond initial dataset, precision, recall, F1.

architecture	augmented dataset	precision		recall		F1-score		mean IoU	
		ROI	backgrd	ROI	backgrd	ROI	backgrd	ROI	backgrd
FCN-8s	initial	0.6178	0.7142	0.6711	0.7110	0.6411	0.7104	0.6128	0.8149
	+replica(G0)	0.6788	0.7632	0.7089	0.7452	0.6918	0.7526	0.6524	0.8325
	+shape(G1)	0.7475	0.8153	0.7569	0.7852	0.7515	0.7992	0.6912	0.8550
U-Net	initial	0.7221	0.7908	0.8260	0.8552	0.7647	0.8192	0.6703	0.8647
	+replica(G0)	0.8108	0.8700	0.8573	0.8682	0.8326	0.8688	0.7361	0.8835
	+shape(G1)	0.8455	0.8951	0.8721	0.8789	0.8581	0.8865	0.7639	0.8925
SegNet-VGG16	initial	0.9950	0.9926	0.9808	0.9805	0.9877	0.9862	0.8669	0.9447
	+replica(G0)	0.9754	0.9858	0.9663	0.9675	0.9708	0.9765	0.8516	0.9398
	+shape(G1)	0.9997	0.9999	0.9932	0.9936	0.9964	0.9967	0.9209	0.9695
DeepLabv3+ ResNet18	initial	0.9491	0.9679	0.9287	0.9309	0.9387	0.9489	0.8334	0.9303
	+replica(G0)	0.9695	0.9713	0.8335	0.8855	0.8929	0.9252	0.7932	0.9212
	+shape(G1)	0.9774	0.9864	0.9549	0.9554	0.9660	0.9705	0.8523	0.9387
DeepLabv3+ ResNet50	initial	0.9945	0.9972	0.9701	0.9711	0.9821	0.9839	0.8889	0.9558
	+replica(G0)	0.9843	0.9805	0.8539	0.9064	0.9112	0.9406	0.8088	0.9292
	+shape(G1)	0.9980	0.9991	0.9814	0.9815	0.9896	0.9902	0.9042	0.9622

Table 2 shows the predicted results applied on the initial trained networks and another synthetic augmented trained network using our replica and shape synthetic augmentation methods. Viewing on the FCN-8s, SegNet-VGG16, and DeepLabv3+ based on ResNet18 and ResNet50, our replica and shape synthetic augmentation methods can perform higher-precision index value from the viewpoint of the nuclei-ROI and background. Moreover, the FCN-8s and SegNet-VGG16 indicate the higher recall index value. These lead to the higher F1-score and mean IoU. Thus, we

promised that the shape synthetic augmentation method toward the test dataset is effective for the base architectures.

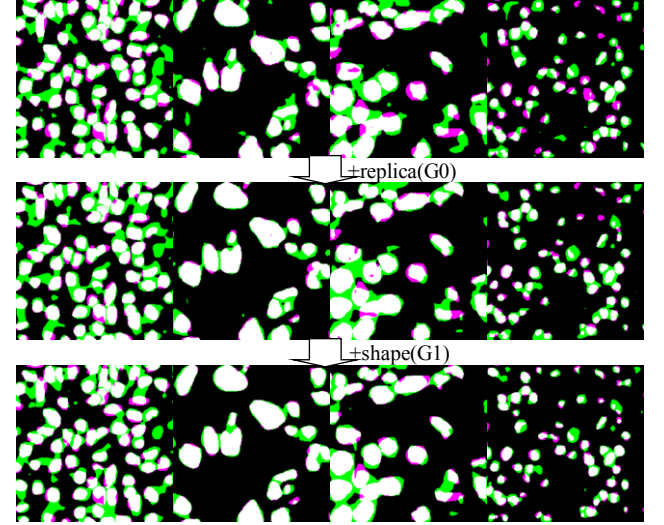


Figure 9: Overlay between ground truth and FCN-8s predicted mask, the initial segmentation (top) with our replica augmentation (middle), and shape synthetic augmentation (bottom).

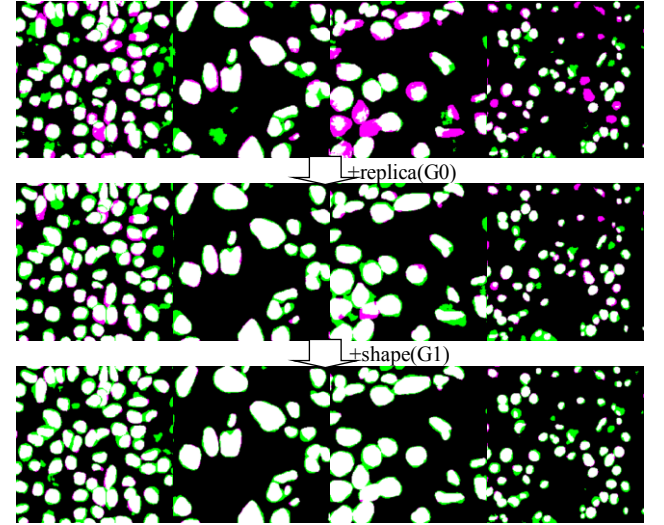


Figure 10: Overlay between ground truth and U-Net predicted mask, the initial segmentation (top) with our replica augmentation (middle), and shape synthetic augmentation (bottom).

3.5. Predict test images partitioned initial dataset

Figure 9 shows the overlay of two labels between the ground truth region of nuclei interest and the predicted region by the FCN-8s trained segmentation networks. The white region is good prediction to match between the ground truth and the nuclei prediction. In contrast, the green region is over precision and the magenta region is less recall. From top to bottom, the first output stands for the initial dataset based prediction, next, the middle result denotes our replica synthetic augmented prediction. At the bottom, it

indicates our shape synthetic augmented prediction. Compared these predicted results, using our shape synthetic augmentation method, their extra-predicted green region and less-recall region are decreasing gradually.

In the same manner, Figure 10 and 11 shows the nuclei predicted results by the trained U-Net, SegNet-VGG16 respectively. Further, Figure 12 shows the predicted results by the trained DeepLabv3+ResNet50. Therefore, the shape synthetic augmentation methods can always reduce the green region (over-precision) and the magenta region (less-recall), so it enables to maximize the white region (accurate prediction to match the ground truth) on these base architectures of semantic segmentation algorithms.

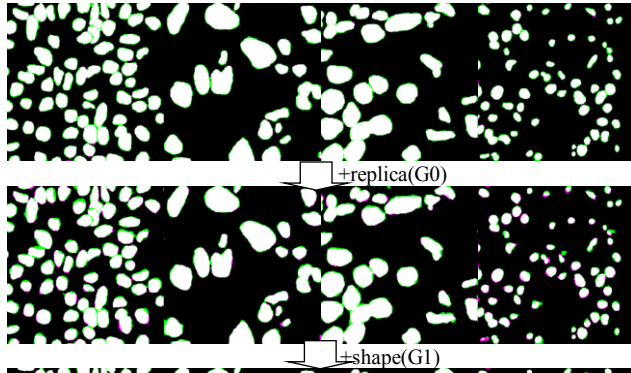


Figure 11: Overlay between ground truth and SegNet-VGG16 predicted mask, the initial (top) with our replica augmentation (middle), and our shape synthetic augmentation (bottom).

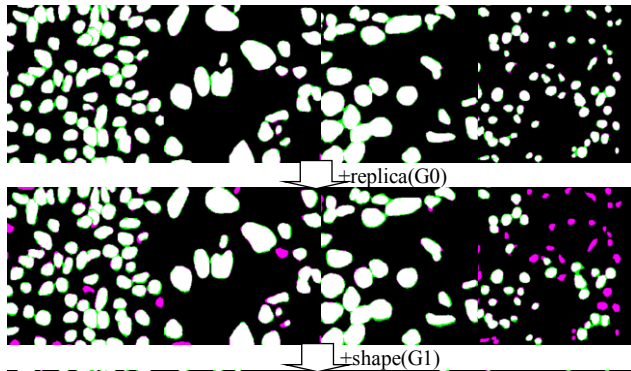


Figure 12: Overlay between ground truth and DeepLabv3+ResNet50 predicted mask, to compare the initial segmentation

(top) with our replica synthetic augmentation (middle), and our shape synthetic augmentation (bottom).

4. Conclusion

4.1. Concluding remarks

This paper proposes a synthetic augmentation procedure using L1-Conditional GAN. This is an image-to-image translation algorithm, which maps tri-categorized labels to real tumor images. Their tri-labels consist of the region of interest (ROI), structure edge, and the background. We propose a Canny edge to extract the feature of structure edge from photos such as stain tissue images. We demonstrated a synthetic augmentation procedure using L1-Conditional GAN applied to datasets for semantic segmentation. We demonstrated that predicted results using our the shape synthetic augmentation methods are possible to improve the segmentation accuracy over several base architectures, such as FCN-8s, U-Net, SegNet-VGG16, and DeepLabv3+ResNet50. From a performance merit of view, our synthetic augmentation methods can reduce the green region (over-precision), and hence it improves the precision accuracy of several segmentation algorithms.

4.2. Future works

We aim to tackle the development of a more general-purpose diagnosis application for digital pathology. This paper focused on the nuclei segmentation dataset in tumor images at the stained tissue. We applied our generative synthetic augmentation methods to the basic five architectures, instead more general feasibility study remains to be conducted toward recent refined pathology architectures. There are opportunities to apply other nuclei segmentation of malignant on different disease slides images. Furthermore, another what-if type augmentation study remains, for example, malignant scenario augmentation what if new tumor occurred on benign images.

[Acknowledgments] I would like to thank Takuji Fukumoto and Shinichi Kuramoto (MathWorks Japan) for providing us MATLAB resources for deep learning frameworks.

(Preprint submitted April 22, 2020)

References

- [1] Wang, S., Yang, D.M., Rong, R. et al., Pathology Image Analysis Using Segmentation Deep Learning Algorithms, American Journal of Pathology, Vol.189, No.9, 2019.
- [2] Shelhamer, E., Long, J., Darrell, T., Fully Convolutional Networks for Semantic Segmentation, IEEE Trans Pattern Anal Mach Intell, 39, pp640-651, 2017.
- [3] Ronneberger, O., Fischer, P., Brox, T., U-Net: Convolutional Networks for Biomedical Image Segmentation, edited by

- Navab, N. et al. In Medical Image Computing and Computer-Assisted Intervention (MICCAI) 2015, Springer, pp234-241, 2015.
- [4] Badrinarayanan, V., Kendall, A., Cipolla, R., SegNet: A Deep Convolutional Encoder-decoder Architecture for Image Segmentation, IEEE Trans Pattern Anal Mach Intell, 39, pp2481-2495, 2017.
- [5] Chen, L.C., Papandreou, G., Kokkinos, I. et al., DeepLab: Semantic Image Segmentation with Deep Convolutional Nets, Atrous Convolution, and Fully Connected CRFs, IEEE Trans Pattern Anal Mach Intell, 40, pp834-848, 2018.
- [6] Lahiani, A., Gildenblat, J., Klamann, I. et al., Generalizing Multi-stain Immunohistochemistry Tissue Segmentation using On-shot Color Deconvolution Deep Neural Networks, 2018, arXiv:1805.06958v3.
- [7] Graham, S., Rajpoot, N., SAMS-NET: Stain-aware Multi-scale Network for Instance-based Nuclei Segmentation in Histology Images, April, 2018, DOI:10.1109/ISBI.2018.8363645.
- [8] Cui, Y., Zhang, G., Liu, Z. et al., A Deep Learning Algorithm for One-step Countour Aware Nuclei Segmentation of Histopathological Images, 2018, arXiv:1803.02786v1.
- [9] Kumar, N., Verma, R., Sharma, S. et al., A Dataset and a Technique for Generalized Nuclei Segmentation for Computational Pathology, IEEE Transaction on Medical Imaging, Vol.36, No.7, 2017.
- [10] Alom, M.Z., Aspinas, T., Taha, T.M. et al., Advanced Deep Convolutional Neural Network Approaches for Digital Pathology Image Analysis: A Comprehensive Evaluation with Different Use Cases.
- [11] Chan, L., Hosseini, M.S., Rowsell, C. et al., HistSegNet: Semantic Segmentation of Histological Tissue Type in Whole Slide Images, pp10662-10671, ICCV2019.
- [12] Graham, S., Chen H., Gamper, J. et al., MILD-Net: Minimal Information Loss Dilated Network for Gland Instance Segmentation in Colon Histology Images, Medical Image Analysis, 2018.
- [13] Dabass, M., Vashisth, S., Review of Histopathological Image Segmentation via current Deep Learning Approaches, May 2019: DOI:10.1109/CCAA.2018.8777616.
- [14] Hindupur, A., The GAN Zoo, <https://github.com/the-gan-zoo>.
- [15] Yi, X., Walia, E., Babyn, P., Generative Adversarial Network in Medical Imaging: A Review, arXiv:1909.07294v4.
- [16] Singh, V., Abdel-Nasser, M., Rashwan, H. et al., FCA-Net: Adversarial Learning for Skin Lesion Segmentation Based on Multi-scale Features and Factorized Channel Attention, DOI:10.1109/ACCESS.2019.2940418, IEEE Access.
- [17] Sirmacek, B., Kivits, M., Semantic Segmentation of Skin Lesion using A Small Data Set, arXiv:1910.10534v1.
- [18] Kazeminia, S. et al., GANs for Medical Image Analysis, arXiv:1809.06222.
- [19] Frid-Adar, M., Diamant, I. et al, GAN-based Synthetic Medical Image Augmentation for increased CNN Performance in Lesion Classification, CVPR, 2018.
- [20] Isola, P., Zhu, J-Y. et al., Image-to-image Translation with Conditional Adversarial Network, CVPR, 2017.
- [21] Gonzalez, R.C., Woods, R.E. : Digital Image Processing, 4th Global Edition, Pearson.
- [22] The Cancer Genome Atlas, accessed on March 26, 2020. <https://www.cancer.gov/about-nci/organization/ccg/research/structural-genomics/tcga>.
- [23] Zhou, S.K., Greenspan, H., Shen, D., Deep Learning for Medical Image Analysis, The Elsevier and MICCAI Society Book Series, Academic Press, 2017.
- [24] Kumer, V., Abbas, A.K., Aster, J.C., Robbins Basic Pathology 10th edition, Elsevier, 2018.
- [25] Foster, D., Generative Deep Learning: Teaching Machines to Paint, Write, Compose and Play, O'Reilly, 2019.

5. Appendix

5.1. Training process under the initial dataset

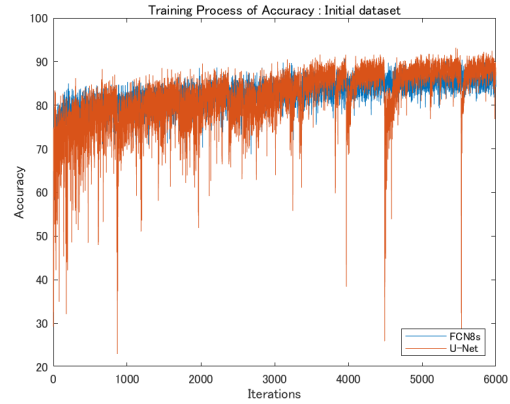


Figure 13: Training process of accuracy under the initial dataset, learning by FCN-8s, U-Net.

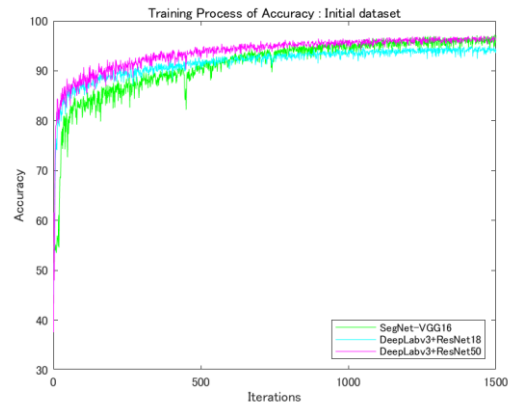


Figure 14: Training process of accuracy under the initial dataset, learning by SegNet-VGG16, DeepLabv3+ResNet18, ResNet50.

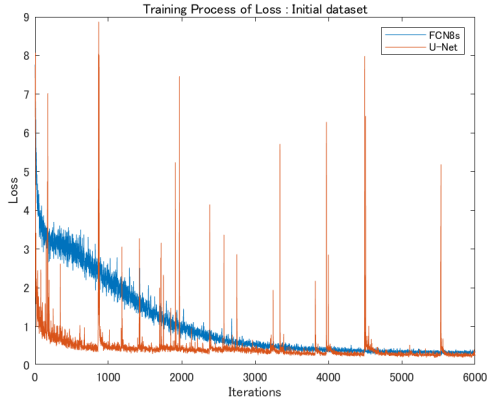


Figure 15: Training process of loss under the initial dataset, learning by FCN-8s, U-Net.

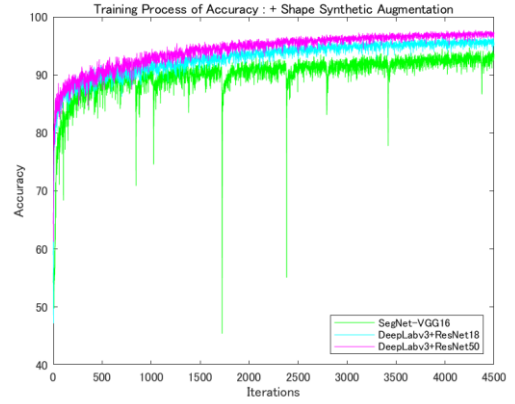


Figure 18: Training process of accuracy using shape synthetic augmentation, learning by SegNet-VGG16, DeepLabv3+ResNet18, ResNet50.

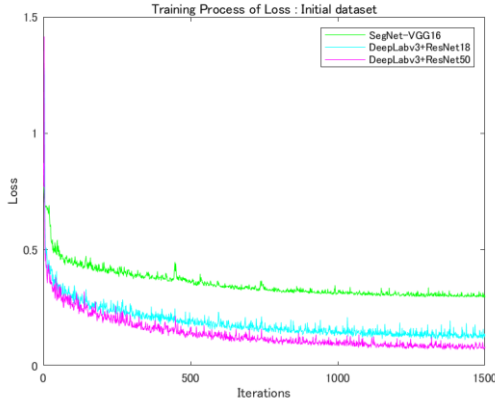


Figure 16: Training process of loss under the initial dataset, learning by SegNet-VGG16, DeepLabv3+ResNet18, ResNet50.

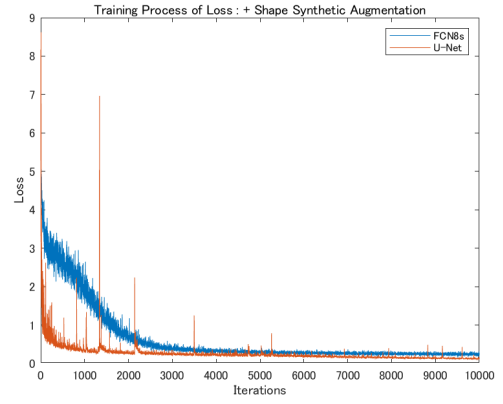


Figure 19: Training process of loss using shape synthetic augmentation, learning by FCN-8s, U-Net.

5.2. Training process using shape synthetic augmentation

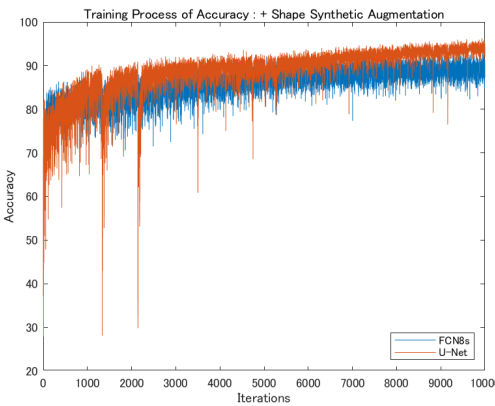


Figure 17: Training process of accuracy using shape synthetic augmentation, learning by FCN-8s, U-Net.

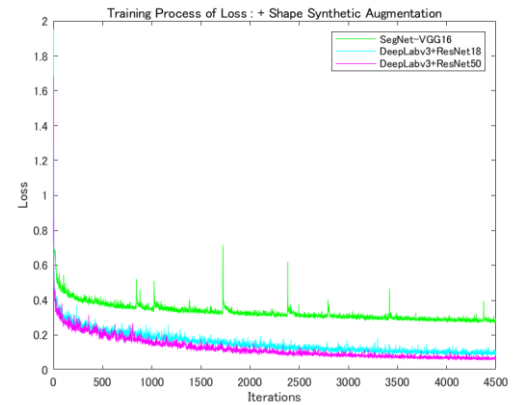


Figure 20: Training process of loss using shape synthetic augmentation, learning by SegNet-VGG16, DeepLabv3+ResNet18, ResNet50.